Conference on Modelling Fluid Flow (CMFF'25)
The 19th International Conference on Fluid Flow Technologies
Budapest, Hungary, August 26 - August 29, 2025

COMBUSTION- AND POLLUTANT-MODELLING OF DIMETHYL ETHER IN A SWIRL-STABILIZED COLD AIR BURNER

Moritz DIEWALD[1], Leona GÖHLER[2], Nico SCHMITZ[2], Christian WUPPERMANN[2]

[1] Corresponding Author. Department for Industrial Furnaces and Heat Engineering, RWTH Aachen University. Kopernikusstraße 10, 52074 Aachen, Germany. E-mail: diewald@iob.rwth-aachen.de
[2] Department for Industrial Furnaces and Heat Engineering, RWTH Aachen University

ABSTRACT

The European Green Deal aims to make Europe the first climate-neutral continent by 2050, emphasizing the transformation of energy systems towards affordability, efficiency and circularity. Within this context, biofuels like renewable Dimethyl Ether (rDME) are pivotal in reducing carbon footprints by replacing fossil fuels. Dimethyl Ethers (DME) advantage over hydrogen lies in its transportability and combustion properties, making it a viable alternative for energy-intensive industries such as steel industry.

As part of the EU-funded "Butterfly" project, DME is synthesized from organic residues using advanced processes like Sorption Enhanced DME Synthesis (SEDMES). This method positions DME as a carbon-neutral biofuel option when derived from syngas produced through organic waste materials. [1]

This paper explores various simulation approaches for DME combustion within a swirl-stabilized cold air burner and compares them with experimental data obtained from an in-house test stand. The study focuses on key parameters such as exhaust gas composition, furnace temperature and the energy balance within the furnace. Particular attention is given to air pollutants like nitrous monoxide (NO) and carbon monoxide (CO).

The results offer insights into how conventional burners designed for natural gas and propane respond when fired with DME and contribute to understanding how renewable fuels can be integrated into existing infrastructure while meeting stringent environmental standards. By comparing simulated outcomes with real-world data, this research supports the transition towards cleaner energy sources in line with global climate goals.

Keywords: CFD, Combustion, dimethyl ether, pollutant formation, RANS

NOMENCLATURE

$\dot{H}$	$[kW]$	enthalpy stream
LHV	$[J/kg]$	lower heating value
M	$[kg/mol]$	molar mass
$\dot{Q}$	$[kW]$	heat stream
T	$[°C]$	temperature
c_p	$[J/K]$	heat capacity at constant pressure
l_{min}	[-]	stoichiometric air-fuel-ratio
m	[-]	stochiometric factor
$\dot{m}$	$[kg/s]$	mass flow
n	[-]	stochiometric factor
o	[-]	stochiometric factor
$o_{2,min}$	[-]	stoichiometric oxygen-fuel-ratio
p	[-]	stochiometric factor
q	[-]	stochiometric factor
r	[-]	stochiometric factor
λ	[-]	air-fuel-equivalence-ratio

Subscripts and Superscripts

DME	regarding DME
air	regarding air
combustion	regarding enthalpy of combustion
cool	regarding cooling air
in	streaming in
off-gas	regarding off-gas
out	streaming out
wall	regarding wall
$\bar{}$	averaged over relevant temperature range

1. INTRODUCTION

The exploration of renewable alternatives to fossil fuels is a subject of current research. The transition to renewable alternatives is indispensable to achieve the goals of the Paris Climate Agreement. However, the use of chemical energy carriers remains the state of the art, especially for energy-intensive processes that require high spatial energy

density. Current research is therefore focused on how fossil fuels like natural gas (NG) or liquefied petroleum gas (LPG) can be replaced by renewable alternatives such as hydrogen (H_2). The paper addresses this research question and examines the use of DME as a fuel in a conventional cold air burner. Focus is placed on the effects of DME combustion on the formation of air pollutants such as NO or CO.

The simulation of combustion processes is very computationally intensive, as it requires modelling not only the flow field but also a temperature field and reaction kinetics. Reaction modelling can be realized through various approaches. This paper examines the results of Flamelet Generated Manifold (FGM) combustion modelling. It then compared the results of different kinetic mechanisms and different NO-postprocessing approaches and compares them with experimental data obtained from a burner test stand.

2. METHODOLOGY

In this work, different combustion simulations are conducted and compared with measurements from a burner test stand.

Similar studies have already been carried out in a previous conference paper by this author [2]. However, in that case, the combustion modelling was performed using an adiabatic FGM. One conclusion of that study was to simulate the combustion using a non-adiabatic FGM matrix to achieve more accurate results regarding NO- and CO-concentrations in the exhaust gas. Additionally, other kinetic mechanisms such as those proposed by Li et al. [3] should be considered. [2]

Besides optimising the combustion simulation, a more precise simulation of heat losses through cooling should also be pursued. [2]

2.1 Combustion Calculation

With the help of combustion calculations, theoretical values for the exhaust gas composition of the main reaction products can be determined. The basis for this calculation is Eq. (1) [4].

$$C_m H_n O_o + \left(m + \frac{n}{4} - \frac{o}{2}\right) O_2 \rightarrow mCO_2 + \frac{n}{2} H_2O \quad (1)$$

Here, it is assumed that carbon atoms fully react to carbon dioxide (CO_2) and hydrogen atoms fully react to water (H_2O). This simplification is possible because it involves a fuel-lean combustion where unburned oxygen (O_2) is found in the exhaust gas.

From Eq. (1), Eq. (2) [4] can be derived to determine the stoichiometric oxygen-fuel-ratio.

$$o_{2,min} = m + \frac{n}{4} - \frac{o}{2} = 3 \quad (2)$$

with

$m = 2$
$n = 6$
o $= 1$

For pure DME combustion, this results in a stoichiometric oxygen-fuel-ratio of 3 mol_{O2}/mol_{DME}. With a simplified air composition of 21 *vol.-%*, the stoichiometric oxygen-fuel-ratio can be converted into the stoichiometric air-fuel-ratio using Eq. (3) [4].

$$l_{min} = \frac{3}{0{,}21} = 14{,}29 \quad (3)$$

The stoichiometric air-fuel-ratio for DME is thus 14,29 mol_{air}/mol_{DME}.

In the next step, based on the given power and air ratio, the required mass flows for fuel and combustion air are calculated. The experiments discussed in this paper are operated at a power of 30 *kW* and an air-fuel-equivalence-ratio of 1,1. Using the known lower heating value (LHV_{DME} = 16,46 kWh/m^3) from Teng et al. [5], Eq. (4) [4] yields a fuel mass flow rate of 0,001039 *kg/s*.

$$\frac{\dot{H}_{\mathrm{combustion}}}{LHV_{\mathrm{DME}}} = \dot{m}_{\mathrm{DME}} = 0{,}001039 \frac{kg}{s} \quad (4)$$

Based on the known stoichiometric air-fuel-ratio, together with the air-fuel-equivalence-ratio, Eq. (5) [4] results in an air mass flow rate of 0,01028 *kg/s*.

$$l_{min} \cdot \lambda \cdot \dot{m}_{\mathrm{DME}} \cdot \frac{M_{\mathrm{air}}}{M_{\mathrm{DME}}} = \dot{m}_{\mathrm{air}} = 0{,}01028 \frac{kg}{s} \quad (5)$$

These mass flows ensure consistent energy input for both numerical modelling and investigations at the test stand. The same combustion values are set for both simulations and burner tests to compare numerical modelling results with test stand experiments effectively.

Additionally, using known mass flows and combustion reactions, a theoretical exhaust gas composition can be calculated. Eq. (6) [4] shows the adjusted reaction equation for a fuel-lean combustion with correct exhaust ratios.

$$C_2H_6O_1 + p\ O_2 + q\ N_2 \rightarrow 2CO_2 + 3H_2O + r\ O_2 + q\ N_2 \quad (6)$$

with

$$p = \lambda \cdot o_{2,min}$$
$$q = \lambda \cdot o_{2,min} \cdot \frac{0{,}79}{0{,}21}$$
$$r = (\lambda - 1) \cdot o_{2,min}$$

These chemical considerations result in a calculated moist exhaust gas composition, which is shown in Chapter 3, along with measurement and simulation results.

2.2 Test stand

The combustion chamber has a square base with a side length of 640 *mm*. The height of the combustion chamber is 1000 *mm*. Figure 1 shows a cross-section through the middle of the combustion chamber.

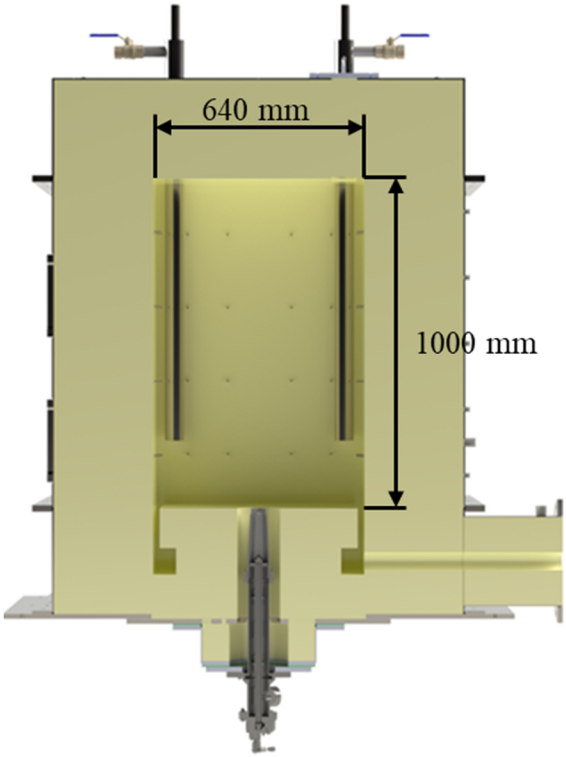

Figure 1. Cut through the burner test stand

The burner, type BIC HB65 by Honeywell [6], is mounted firing upwards in the centre of the bottom plate. At the top of the combustion chamber, four cooling tubes are installed. These are air-cooled to establish a load condition, allowing the test stand to reach a steady state.

The cooling tubes are designed as a pipe-in-pipe construction. Cool air flows in through the outer tube and out again through the shorter inner tube. The lower end of the outer pipe is welded shut so that the oven atmosphere and the cooling air are not mixed. The heat flux of the cooling air corresponds to the power acting on the process or product in an industrial furnace. The cooling tubes are cylindrical with a diameter of 60 *mm* and a length of 800 *mm*. The central axis of the cooling tubes is positioned at 56 *mm* from the wall.

The square bottom plate has a side length of 600 *mm*, creating a gap of 20 *mm* through which exhaust gases can be extracted from the combustion chamber. The extraction is controlled to maintain a constant furnace pressure of 35 *Pa*. The test stand is insulated with a 300 *mm* thick refractory layer.

The off-gas concentration measurements are performed using different measurement systems. The Ultrakust Hygrophil H 4230-10 is uses psychrometric humidity measurement to measure the wet off gas concentration of H_2O. The other concentrations in the off gas are measured in the dry offgas. An Emerson X-Stream measures CO and CO_2 concentration using a Non-Dispersive Infrared (NDIR) Sensor and O_2 using a paramagnetic sensor. An Emerson CLD is used to measure the NO_X-Concentration using Chemiluminescence.

In experiments at the burner test stand, besides measuring exhaust gas composition and temperature, both volumetric flow rate and temperatures of the cooling air before and after passing through the cooling tubes are measured.

Additionally, the wall temperature is measured at mid-height on the inner side of the refractory material. All thermocouples used were of type N class 1. At temperatures over 1100 *°C* the error of these thermocouples is rounded up to 2 *K*.

The volume flow of the cooling air is measured using a pitot tube. The measurement uncertainty results in an error of 1 *Pa*.

2.3 Energy Balance

From the values measured in the test stand, along with the known mass flows from Section 2.1, the exhaust gas enthalpy and the enthalpy difference of the cooling air can be calculated. The enthalpy input from the heat of combustion air and fuel gas is neglected due to low entry temperatures. The energy flows considered are shown in Figure 2.

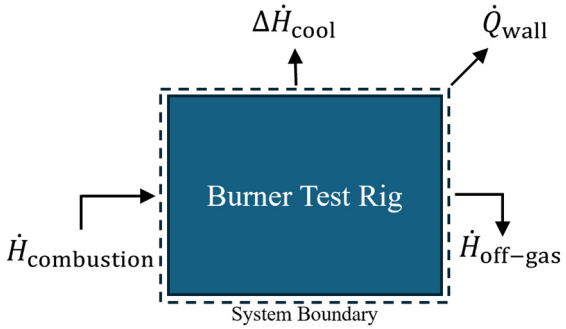

Figure 2. Energy Balance (after [7])

Previous experiments have demonstrated that a steady state can achieved with a cooling air heat flux of around 8 *kW*. The test stand and simulation boundary conditions are set accordingly. Based on the considered energy streams, an energy balance of the furnace can be established. Thus, the energy balance can be calculated using Eq. (7).

$$\dot{H}_{\text{combustion}} = \dot{H}_{\text{off-gas}} + \Delta\dot{H}_{\text{cool}} + \dot{Q}_{\text{wall}} \tag{7}$$

The combustion enthalpy amounts to 30 *kW* and remains constant for all experiments. The exhaust gas enthalpy is determined according to Eq. (8), where the average heat capacity is determined based on each measured exhaust concentration according to VDI 4670 (2016) [8].

$$\dot{H}_{\text{off-gas}} = (\dot{m}_{\text{DME}} + \dot{m}_{\text{air}}) \cdot \bar{c}_{p,\text{off-gas}} \cdot \left(T_{\text{off-gas,out}} - T_0\right) \tag{8}$$

The off-gas enthalpy is calculated in this way for the test stand and the simulation data.

The cooling air enthalpy difference is calculated using Eq. (9).

$$\Delta\dot{H}_{\text{cooling}} = \dot{m}_{\text{cool}} \cdot \bar{c}_{p,\text{air}} \cdot \left(T_{\text{cool,out}} - T_{\text{cool,in}}\right) \tag{9}$$

The average heat capacity is also determined according to VDI 4670 (2016) [8].

Additionally, wall losses are compared, although they are difficult to determine experimentally. Therefore, they are only calculated from the energy balance for experiments.

2.4 Mesh and Boundary Conditions

The simulation volume exactly corresponds to that of the test stand. It begins 30 *mm* below the swirl plate and ends in the exhaust channel 75 *mm* below the base plate. The exhaust channel is simulated to this extent to prevent backflow.

The mesh is based on a poly-hexcore mesh and is created using ANSYS© Fluent. Firstly, a grid independence study is performed. Therefore, the cell sizes are varied. In the coarsest mesh the largest hexahedra have an edge of 20 *mm*, with the finer meshes having maximum cell lengths of 16 mm, 14,4 *mm* and 12,8 *mm* respectively. A simulation is performed for all four mesh sizes and the temperature over different hights is compared. Figure 3 shows the temperature over the height along the burner axis.

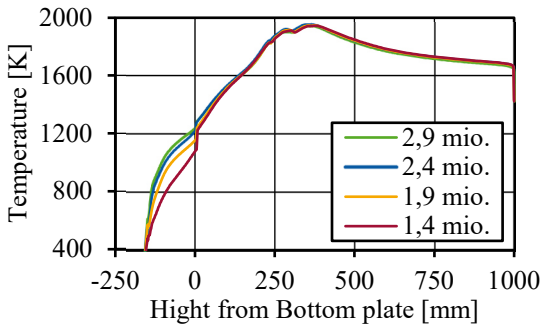

Figure 3. Temperature over the height along the burner axis

After the grid independence study the 2,4 mio. cell mesh is chosen as the temperature curve deviates only slightly from the 2,9 mio. cell mesh. The 2,4 mio. cell mesh corresponds to a maximum edge length of 14,4 *mm*. The mesh includes five mesh refinement levels that are determined based on the flame shape. Consequently, the smallest cells within the swirl plate have a size of 0,45 *mm*. Figure 4 shows the simulation geometry and the form of the mesh refinement levels.

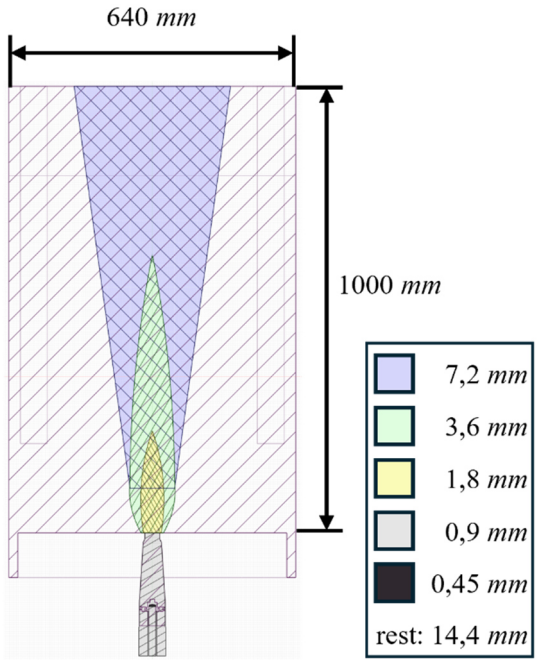

Figure 4. Simulation Geometry and Mesh Refinement

The outer walls of the combustion chamber are simulated using one-dimensional heat conduction with external convection. The conduction consists of two layers. An inner layer representing the refractory material with a thickness of 300 *mm* and an outer layer modelled after the 15 *mm* thick steel body of the test stand. The external temperature is assumed to be 300 *K*. The burner walls and the inner side of the exhaust channel are assumed as adiabatic. The

cooling tubes are assumed to have a constant heat flux, resulting in the previously defined cooling capacity of 8 *kW*. The fuel and air temperatures are 300 *K*.

2.5 Numerical Modelling

The simulations in this work are conducted using the commercial simulation software ANSYS© Fluent 2024R2. The simulations are Reynolds-Averaged Navier-Stokes (RANS) simulations.

Previous simulations showed that the k-omega SST turbulence model [9] generates unsteady flow fields that negatively affect combustion modelling. For this reason, the realizable k-epsilon model [10] was selected for the simulations in this study. Radiation is represented using a 4x4 Discrete Ordinates model [11–13].

Combustion modelling, alongside the choice of kinetic mechanism, is an important consideration in combustion calculations. There are various modelling approaches that differ in accuracy and computational time.

In this paper, combustion is modelled using the Flamelet Generated Manifold (FGM) model [14], which is coupled with a presumed-shape Probability Density Function (PDF) to capture turbulence-chemistry interaction.

Two simulations with different kinetic mechanisms are performed. One simulation is based on the mechanism by Prince et al. [15,16] and the other on the mechanism by Li et al. [3]. Further comparisons between these mechanisms can be found in the preceding paper [2].

The spatial discretisation becomes more complex with increasing simulation accuracy. The final simulation uses the PRESTO! algorithm for pressure interpolation and a first-order upwind scheme for radiation calculation. The other transport equations are solved using a second-order upwind scheme.

2.6 NO-Post-Processing

The FGM model resolves only the twelve most significant species by proportion, so NO is not calculated. Therefore, various post-processing calculations were conducted to determine the NO concentration. These transport equations are post-processed from converged combustion simulations. This approach is valid, as the NO concentration is minuscule compared to the main combustion products.

For this work, three approaches to NO modelling integrated in ANSYS© Fluent were selected:

1. NO_X Modelling (NO_X)
2. Decoupled Detailed Chemistry (DDC)
3. Reactor Network Modelling (RNM)

The ANSYS© Fluent NO_X model used in this work simulates thermal and prompt NO_X formation. NO_X prediction is achieved by solving transport equations for NO and intermediate nitrous oxide (N_2O). The incorporated rate models originate from the Department of Fuel and Energy at the University of Leeds and open literature. [17]

The Decoupled Detailed Chemistry Model in Fluent is based on the same idea as the NO_X model. However, instead of using rate models embedded in Fluent, any kinetic mechanisms can be loaded. [17]

The reactor network model simulates species and temperature fields in a combustor using detailed chemical kinetics. A kinetic mechanism is imported and solved within the reactor network. Therefore, the combustor is divided into a few perfectly stirred reactors, with mass fluxes determined from the CFD solution. This approach efficiently captures finite-rate chemistry effects, particularly for NO, CO and unburnt hydrocarbons. Since the number of reactors is much smaller than the cells of the mesh, it allows faster simulations. [17]

The kinetic mechanism and combustion modelling approaches used in this work are listed in Table 1. The converged FGM combustion simulation before post-processing is labelled as FGM.

Table 1. List of combustion models

No.	Name	Combustion Model	Kin. Mech.
1	FGM Prince	FGM	Prince [15,16]
2	NOX Prince	NOX	Prince [15,16]
3	DDC Prince	DDC	Prince [15,16]
4	RNM Prince	RNM	Prince [15,16]
5	FGM Li	FGM	Li [3]
6	NOX Li	NOX	Li [3]

Only the Prince mechanism includes NO_X chemistry. Therefore, DDC and RNM which are based on the chosen kinetic mechanism are only used in combination with the Prince kinetic mechanism.

3. RESULTS AND DISCUSSION

When switching from natural gas to pure DME combustion, the burner shut off repeatedly. To ensure a stable combustion, a minimal volume flow of 3,15E-7 *kg/s* natural gas is added constantly. This results in a DME concentration of 99,9 *Vol.-%* in the fuel. Further trials must be performed to test if the malfunction arises from the burner itself or the burner control system. The simulated combustion asumes 100 *Vol. %* DME nonetheless.

Table 2 illustrates the temperatures from the simulations and test stand experiments. The FGM

Prince simulation deviates by 35 *K*. The exhaust temperature is overestimated, with a deviation of 23 *K*. The RNM Prince simulation results in the highest temperatures, with both exhaust and wall temperatures at 1209 *K*, exceeding measured values by 96 *K* and 65 *K*, respectively. The FGM Li simulations also demonstrate higher temperatures than those recorded in the test stand, with exhaust temperature being 60 *K* and wall temperature 67 *K* above the measurements.

Table 2. Results of Temperature

	$T_{\text{off-gas}}$ [°C]	T_{wall} [°C]
Trial	1113±2	1144±2
FGM Prince	1136	1179
RNM Prince	1209	1209
FGM Li	1173	1211

There could be various reasons for these deviations. One possible reason could be inaccurate modelling of the wall and cooling tubes heat-fluxes or a not fully heated test stand. Another reason with regards to the off-gas temperature are the differing measurement positions between experiments and simulations leading to larger discrepancies in the exhaust channel.

Next, the temperature fields are displayed. Therefore, a plane is placed diagonally along the burner axis so that it cuts through the centres of two cooling tubes. Figure 5 displays the temperature field of the FGM Li simulation. As the temperature field of the FGM Prince simulation is very similar it is not shown.

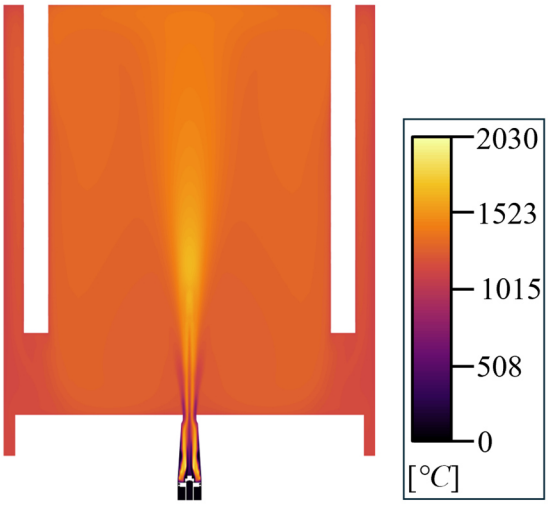

Figure 5. Temperature Field of FGM Li

The temperature before the burner swirl plate is the lowest. In the area after the burner swirl plate the temperatures in the centre and at the outer wall are the coolest. Between these cooler areas is a high-temperature zone. This is explained through the mixing of fuel and air. Fuel is injected in the centre of the swirl-plate and air is injected along the outside. As the combustion can only take place if mixture between air and fuel takes place, it makes sense that the hot zones are between these zones. Therefore, the outer cold zone corresponds to an air-rich area and the inner cold zone corresponds to a fuel rich area. After the burner orifice the colder outer layer diffuses outwards, whereas the hotter layer narrows to a point as it consumes the fuel inside the central colder layer. At one point, the outer hot layer separates from the hot zone. Inside this separation a second hot zone begins. This layer not as clearly defined but it diffuses outward reaching its biggest extend right at the tip of the first hot zone and then gradually diffuses so that the hottest area narrows again. Inside this area a secondary reaction takes place. The remaining temperature field has a relative constant temperature except for the temperatures in the corners of the test stand which are shielded from radiation by the cooling tubes.

The energy balance results are presented in Table 3. The values for cooling air enthalpy difference are in good agreement. Exhaust gas enthalpy is well captured in the simulation, even though the measured value is slightly higher. The wall losses are overestimated by the simulations by 1,54 *kW* for the FGM Prince case and 1,75 *kW* for FGM Li.

Table 3. Results of Energy Balance

	$\Delta\dot{H}_{cooling}$ [kW]	$\dot{H}_{offgas}$ [kW]	$\dot{Q}_{wall}$ [kW]
Trial	8,0±0,3	16,4±0,3	5,6±0,4*
FGM Prince	7,94	14,92*	7,14
FGM Li	7,94	14,71*	7,35

*calculated acc. to Eq. (7)

The off-gas enthalpies of the simulation are lower than during the trial. By contrast, the wall losses calculated for the test stand are lower than the wall losses of the simulations. This can either be explained by the inaccurate wall modelling or is a sign, that the steady state of the temperatures inside the test stand wasn't reached when the measurements were taken.

The wet exhaust gas concentrations are detailed in Table 4. The off-gas concentrations for both FGM simulations deviate only by a maximum of 0,1 *vol.-%* from the calculated concentrations. The RNM Prince simulation yields unrealistic results regarding exhaust composition.

Table 4. Off-gas Concentrations

	O_2 [*vol.-%, wet*]	H_2O [*vol.-%, wet*]	CO_2 [*vol.-%, wet*]
Calculated	1,7	16,9	11,3
Trial	1,6±0,3	18,7±0,1	11,0±0,2
FGM Prince	1,7	16,8	11,2
RNM Prince	2,0	10,8	17,6
FGM Li	1,7	16,9	11,3

The comparison of experimental values with calculated ones shows that O_2 and CO_2 concentrations align well. However, H_2O concentrations from experiments exceed those calculated by 2 *vol.-%*. This is an unrealistic deviation. Therefore, the O_2 concentration measurements should be checked for errors and repeated if necessary.

Table 5 presents air pollutants in dry off-gas concentration. The greatest deviation from measured values arises from Decoupled Detailed Chemistry. Here, NO concentration is less than 1 *%* of the measured value, while CO concentration is significantly overestimated at an absolute value of 1,2 *vol.-%*. As discussed in Section 2.6, FGM modelling does not capture NO phase. Prince FGM significantly overestimates CO concentration at 749,5 *ppm*. Since NO_X modelling only considers species involved in NO_X formation (excluding CO), CO concentration also amounts to 749,5 *ppm*. However, the NO concentration closely matches measured values at 54,6 *ppm* compared to 72 *ppm*. Prince RNM underestimates NO concentration by about 61,2 *ppm* while overestimating CO concentration by 35,1 *ppm*.

The FGM Li simulation provides the best results regarding CO concentration with an underestimation of just 4,9 *ppm*. The corresponding NO concentration of the NO_X Li Simulation achieves also good results, with slightly lower-than-expected readings around 35,6 *ppm*.

Table 5. Off-gas Concentrations Pollutants

	NO [*ppm, dry*]	CO [*ppm, dry*]
Trial	72±5	17±3
FGM Prince	-	749,5
NOX Prince	54,6	(749,5)
DDC Prince	0,4	12337,2
RNM Prince	10,8	52,1
FGM Li	-	12,1
NOX Li	35,6	(12,1)

The simulations based on the Prince mechanism tend towards exaggeration when calculating the carbon monoxide emissions. The simulations using the Li mechanism achieve more realistic outcomes.

The NO_X modelling of the NO postprocessing models available in ANSYS© Fluent achieves the most realistic results.

4. SUMMARY

In this paper, two FGM simulations based on different kinetic mechanisms were conducted. Once the simulations reached steady states, various post-processing models were applied to determine NO concentration. The simulation values were compared with test stand measurements in terms of temperature, energy balance and exhaust gas composition.

The burner was not able to combust pure DME. This should be investigated going forward.

Temperatures were overestimated by all simulations. A possible cause could be inaccurate wall and cooling tube boundary conditions or a not fully established steady state during the experiments.

The heat losses from the experiments are comparable to those simulated, although wall losses in the simulation exceed those measured. This suggests inaccurate representation of wall boundary conditions.

When comparing the values of the main exhaust products, it is noticeable that the RNM simulation leads to an unrealistic exhaust composition. The same applies to the water content in the conducted burner trial. All other measurement and simulation values are in good agreement. The measurements should be checked for errors and repeated if necessary.

Regarding air pollutants in the exhaust gas, CO concentration is significantly overestimated by the Prince mechanism. The Li mechanism results in more realistic CO concentrations, which are slightly below those measured. The most realistic simulation results regarding NO concentrations are achieved through NO_X post-processing.

In conclusion, FGM simulation followed by NO_X post-processing and using the Li mechanism leads to the most realistic results. However, it would be of interest to investigate other mechanisms such as those proposed by Khare et al. [18].

The simulation accuracy and validation could be improved further. One improvement could be to measure the outer wall temperatures of the test stand to calculate the wall losses. This could be achieved by using a thermographic camera. It could also be of interest to model the air stream inside the cooling tubes to achieve a spatial distribution of the heat flux through the cooling tube. Additionally, OH* visualisation measurements would be valuable for comparing the flame shape from simulations with that of a real flame.

ACKNOWLEDGEMENTS

Funded by the European Union

This work has been performed as part of BUTTERFLY project which has received funding from the European Union's Horizon Europe Research and Innovation Programme under Grant Agreement No. 101118241.

REFERENCES

[1] Peinado, C., Liuzzi, D., Sluijter, S. N., Skorikova, G., Boon, J., et al., 2024, "Review and perspective: Next generation DME synthesis technologies for the energy transition," *Chemical Engineering Journal*, Vol. 479, p. 147494.

[2] Diewald, M., Kaiser, H., and Schmitz, N., 2024, "Comparison Of Dimethyl Ether And Natural Gas Combustion In A Swirl-Stabilized Industrial Burner," *Selected papers from the 15th International Conference on Industrial Applications of Computational Fluid Dynamics, Trondheim, Norway, June 11–13, 2024,* Trondheim, Norway, pp. 141–148.

[3] Li, Y., Su, S., Wang, L., Yin, J., and Idiaba, S., 2022, "Reduction and optimization for combustion mechanism of dimethyl ether–air mixtures," *International Journal of Chemical Kinetics*, Vol. 54, pp. 142–153.

[4] Pfeifer, H., 2018, *Praxishandbuch Thermoprozesstechnik. Band I: Grundlagen - Prozesse - Verfahren*, Vulkan-Verlag GmbH.

[5] Teng, H., McCandless, J. C., and Schneyer, J. B., 2004, "Thermodynamic Properties of Dimethyl Ether - An Alternative Fuel for Compression-Ignition Engines," *SAE Technical Paper Series,* SAE International.

[6] Honeywell Kromschröder, 2022, "Burners with ceramic tube BIC, BICA, BICW, ZIC, ZICW," URL: https://docuthek.kromschroeder.com/download.php?lang=de&doc=66423&download=1.

[7] Pfeifer, H. (ed.), 2013, *Handbuch industrielle Wärmetechnik. Grundlagen, Berechnungen, Verfahren,* 5th ed., Vulkan Verl., Essen, Ruhr.

[8] Verein Deutscher Ingenieure (VDI), 2016, "Thermodynamische Stoffwerte von feuchter Luft und Verbrennungsgasen: Thermodynamic properties of humid air and combustion gases," 17.200.01, No. 4670 (2016).

[9] Menter, F. R., 1994, "Two-equation eddy-viscosity turbulence models for engineering applications," *AIAA Journal*, Vol. 32, pp. 1598–1605.

[10] Shih, T.-H., Liou, W. W., Shabbir, A., Yang, Z., and Zhu, J., 1995, "A new k-ϵ eddy viscosity model for high reynolds number turbulent flows," *Computers & Fluids*, Vol. 24, pp. 227–238.

[11] Chui, E. H., and Raithby, G. D., 1993, "Computation of radiant heat transfer on a Nonorthagonal mesh using the Finite-Volume-Method," *Numerical Heat Transfer, Part B: Fundamentals*, Vol. 23, pp. 269–288.

[12] Raithby, G. D., and Chui, E. H., 1990, "A Finite-Volume Method for Predicting a Radiant Heat Transfer in Enclosures With Participating Media," *Journal of Heat Transfer*, Vol. 112, pp. 415–423.

[13] Murthy, J. Y., and Mathur, S. R., 1998, "Finite Volume Method for Radiative Heat Transfer Using Unstructured Meshes," *Journal of Thermophysics and Heat Transfer*, Vol. 12, pp. 313–321.

[14] van OIJEN, J. A., and GOEY, L. de, 2000, "Modelling of Premixed Laminar Flames using Flamelet-Generated Manifolds," *0010-2202*, Vol. 161, pp. 113–137.

[15] Prince, J. C., and Williams, F. A., 2015, "A short reaction mechanism for the combustion of dimethyl-ether," *Combustion and Flame*, Vol. 162, pp. 3589–3595.

[16] Mechanical and Aerospace Engineering, Combustion Research, University of San Diego, 2012, "Chemical-Kinetic Mechanisms for Combustion Applications,".

[17] ANSYS, Inc., 2024, "Fluent Theory Guide,".

[18] Khare, R. S., Parimalanathan, S. K., Raghavan, V., and Narayanaswamy, K., 2018, "A comprehensively validated compact mechanism for dimethyl ether oxidation: an experimental and computational study," *Combustion and Flame*, Vol. 196, pp. 116–128.